

# Drag and lift forces on a counter-rotating cylinder in rotating flow

Chao Sun<sup>1</sup>, Tom Mullin<sup>2</sup>, Leen van Wijngaarden<sup>1</sup>, and Detlef Lohse<sup>1</sup>

<sup>1</sup> Physics of Fluids Group, Faculty of Science and Technology, J. M. Burgers Centre for Fluid Dynamics, MESA+ and Impact Institutes, University of Twente, The Netherlands.

<sup>2</sup> Manchester Centre for Nonlinear Dynamics, University of Manchester, Oxford Road, Manchester M13 9PL, United Kingdom.

(Received 29 May 2018)

Results are reported of an experimental investigation into the motion of a heavy cylinder free to move inside a water-filled drum rotating around a horizontal axis. The cylinder is observed to either co- or, counter intuitively, counter-rotate with respect to the rotating drum. The flow was measured with particle image velocimetry (PIV), and it was found that the inner cylinder significantly altered the bulk flow field from the solid-body rotation found for a fluid filled drum. In the counter-rotation case, the generated lift force allowed the cylinder to freely rotate without contact with the drum wall. Drag and lift coefficients of the freely counter-rotating cylinder were measured over a wide range of Reynolds numbers,  $2,500 < Re < 25,000$ , dimensionless rotation rates,  $0.0 < \alpha < 1.2$ , and gap to cylinder diameter ratios  $0.003 < G/2a < 0.5$ . Drag coefficients were consistent with previous measurements on a cylinder in a uniform flow. However, for the lift coefficient considerable larger values were observed in the present measurements. We found the enhancement of the lift force to be mainly caused by the vicinity of the wall.

---

## 1. Introduction

The flow around a rotating cylinder is both of fundamental interest and of importance in many practical applications, such as flow control (Tokumaru & Dimotakis 1991, 1993; Mittal 2003) and the motion of submersed bodies (Davis *et al.* 2007). There have been a number of investigations into the drag and lift forces which act on a rotating cylinder in a uniform flow. For example, Badr *et al.* (1990) report the results of a numerical and experimental study of the influence of the rotation of a cylinder on the flow structure in the wake over Reynolds number range  $10^3$  to  $10^4$  and show significant suppression effects. (The Reynolds number  $Re$  is defined here as  $Re = \frac{u_{fs}d}{\nu}$  where  $u_{fs}$  is the free stream velocity,  $d$  the diameter of the cylinder and  $\nu$  is the kinematic viscosity of the fluid.) Tokumaru & Dimotakis (1991, 1993) demonstrate in a series of experiments, that both the wake structure and drag and lift forces can be controlled by modifying the rotation of a cylinder in a uniform flow. The suppression of vortex shedding by rotation of a cylinder is also reported by Mittal & Kumar (2003) who perform numerical simulations at the relatively low value of  $Re = 200$ . Cliffe & Tavener (2004) perform a numerical bifurcation study of the onset of periodic shedding in a channel and find an exchange between Hopf and pitchfork bifurcations as a function of control parameters. Takayama & Aoki (2004) measured lift and drag coefficients on a rotating cylinder in a flow of  $Re$  from  $0.4 \times 10^5$  to  $1.8 \times 10^5$ . Their results showed that both lift and drag coefficients depend on the dimensionless rotation rate of the cylinder for a fixed  $Re$ . Labraga *et al.*

(2007) measured the separation points on a rotating circular cylinder in cross flow at  $Re$  ranging from 8,500 to 34,000, focusing on the dramatic effect of the exact position of the separation points on the experienced forces. One conclusion which can be drawn from all of these investigations is that large rotation rates can generate significant lift coefficients through the Magnus effect although this is at the cost of the power requirement for rotating the cylinder which increases rapidly with the rotation rate (Mittal & Kumar 2003).

The presence of a wall near a cylinder may significantly change the motion of the object and the forces acting on it. Hu (1995) studied the two-dimensional motion of a freely rotating cylinder in a viscous fluid between parallel walls of a vertical channel, for  $Re$  in the range from 0.01 to 102. He found that when the cylinder moves very close to the channel wall, it rotates in a direction opposite to that of rolling along the wall in contact. When the cylinder is far from the wall, its rotation depends on the value of  $Re$ . Bearman & Zdravkovich (1978) experimentally measured the velocity field and the distribution of mean pressure around a cylinder near a plane boundary at a value of  $Re = 4.5 \times 10^4$ , and found that regular vortex shedding is suppressed, once the gap between the cylinder and the wall is less than about 0.3 cylinder diameters. Sumner & Akosile (2003) and Cao & Tamura (2008) studied the forces on a circular cylinder in uniform shear flow, and found that there is a lift force pointing from the high velocity side towards the low velocity side due to the asymmetrical distribution of pressure around the cylinder. Nishino *et al.* (2007) measured the drag coefficients as a function of the gap to diameter ratio for a non-rotating cylinder at  $Re$  values of  $0.4 \times 10^5$  and  $1.0 \times 10^5$ . They generated a uniform flow in the wall region by using a moving ground for eliminating the boundary layer effect. They found that the drag coefficient gradually decreases as the gap ratio increases, but the dependence is very weak. However, the lift coefficient rapidly increases as the gap to diameter ratio decreases to less than about 0.5 (Nishino *et al.* 2007).

At *low Reynolds numbers*, Ashmore *et al.* (2005); Yang *et al.* (2006) perform experiments with heavy spheres in a rotating cylinder. They observe a cavitation bubble in the lubrication layer between sphere and wall. The presence of a cavitation bubble results in a normal force which balances the gravitational component acting on the sphere (Prokunin 2004; Ashmore *et al.* 2005; Yang *et al.* 2006). Seddon & Mullin (2006) experimentally studied the motion of a heavy cylinder in a rotating cylindrical flow inside a drum in the Stokes flow regime. They observe that the cylinder rotates very slowly either with or against the direction of drum. Again, the cavitation bubbles result in a normal force which balances the effects of gravity of the cylinder. These results are in accord with the theoretical predictions of Jeffrey (1922) (see Jeffrey & Onishi (1981)) who predicts zero rotation of an infinite cylinder translating adjacent to a plane wall in the Stokes limit.

*Large Reynolds number* The aim of the present work is to study the flow characteristics and forces exerted on a cylinder which is rotating freely adjacent to the wall of a rotating fluid-filled drum since this provides a well-defined flow field around the cylinder. The same rotating drum setup has been used by several authors (Naciri 1992; Lohse & Prosperetti 2003; van Nierop *et al.* 2007; Bluemink *et al.* 2008, 2010*a,b*) to determine the lift and drag forces on a light particle or bubble, from its equilibrium position.

Our experiments were carried out in the  $Re$  range between 2,500 and 25,000. In the experimental work discussed above, the force measurements on the rotating cylinder at high  $Re$  were performed on a fixed cylinder, and the rotating rate of the cylinder was controlled externally. In the present experiments, the cylinder moved freely in the flow and its rotation rate was controlled by the flow. The cylinder either co- or counter-rotated depending on the rotating frequency of the drum and the drag and lift forces were determined from the balance of forces acting on the cylinder.

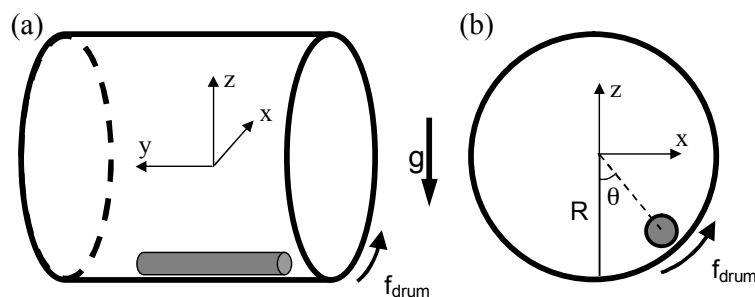


FIGURE 1. A sketch of the experimental setup. (a) Front view and (b) axial view of the apparatus. The direction of gravity is indicated by the downward arrow.

The outline of the paper is as follows. The experimental setup is introduced in Sec. 2. An overview of the rotation rate and sense of rotation of the cylinder are reported in Sec. 3. In Sec. 4, the results of the PIV measurements in the rotating drum are presented, first for the local velocity field around the cylinder, then for the flow field in the whole drum in the absence of the cylinder and subsequently with the cylinder inserted. The results for the drag and lift coefficients are presented in Sec. 5 and some conclusions are drawn in Sec. 6.

## 2. Experiment

Schematic diagrams of front and axial views of the experimental apparatus are given in Fig. 1. The plexiglass drum of length 470 mm and inner radius  $R = 235$  mm was mounted horizontally and leveled with a precision of less than 0.2 degree. Six solid PVC (Polyvinyl chloride) cylinders (made from commercially available extruded PVC cylinders) with density  $1,400 \text{ kg/m}^3$  were used in the experiments. Each was 240 mm long and they were of radii  $a = 7.75, 12.75, 15.5, 20.0,$  and  $30.0$  mm respectively. The cylinders were free to move within the drum, which was filled with de-ionized water. A motor with a feedback loop control was used to drive the drum with an accuracy in the rotation frequency of better than 0.01 Hz. The operating frequency,  $f_{drum}$ , was different for each of the cylinders and typically lay in the range 0.10 Hz to 0.90 Hz.

A paint mark was put on each of the cylinders, as shown in fig. 2 (a, b), in order to measure the angular velocity of the cylinder. The measurements were conducted once the system reached an equilibrium state and this typically took 5 to 10 minutes after each change in  $f_{drum}$ . The rotation of the cylinder was filmed with a high speed camera at a typical frame rate of 250 f.p.s. In general, several periods of the rotation of the cylinder for each  $f_{drum}$  were recorded and the rotation frequency of the cylinder was averaged over the interval.

The azimuthal position of the cylinder in the drum was estimated by firstly aligning the camera with the axis of the drum. The azimuthal angle  $\theta$  was then calculated based on the measured position of the cylinder as illustrated in fig. 3 (a). In order to measure the thickness of the gap between the cylinder and the wall of the drum, the camera was mounted horizontally very close to the cylinder in order to achieve good spatial resolution. Representative images illustrating this procedure are shown in fig. 4 (a, b).

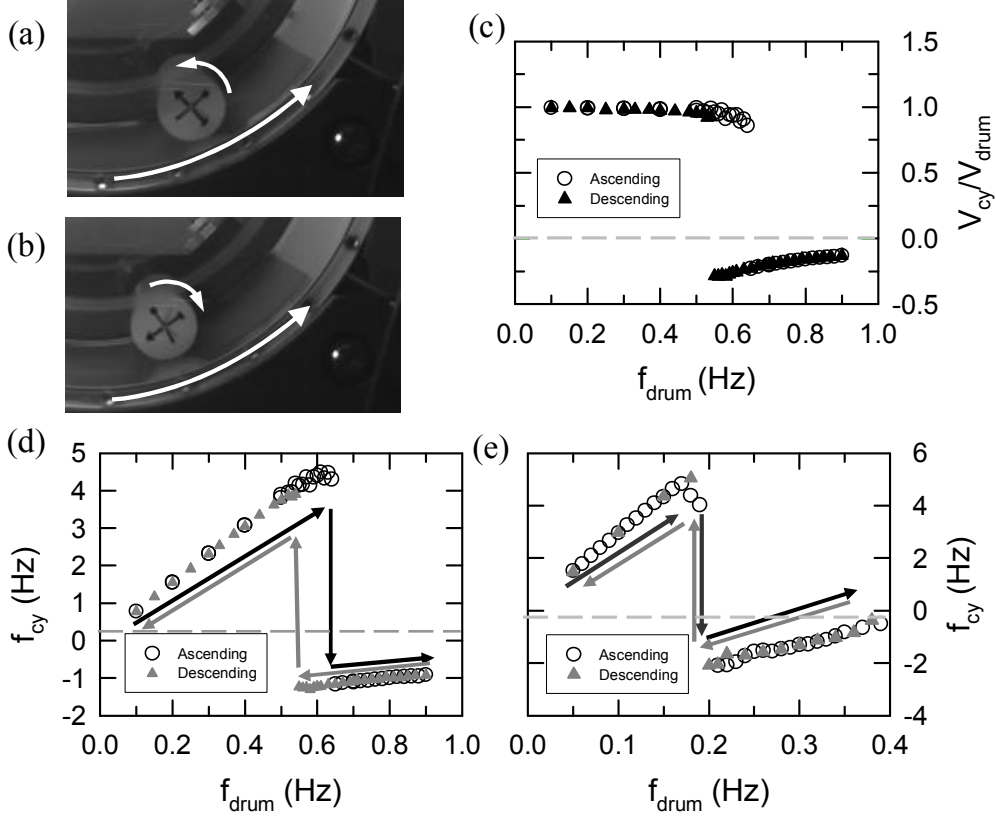


FIGURE 2. Representative frames for the (a) co-rotating ( $f_{drum} = 0.62$  Hz) and (b) counter-rotating ( $f_{drum} = 0.70$  Hz) cylinder ( $a = 30$  mm). Supplementary movies (movie 1 and movie 2) are available for showing the motion of the co- and counter-rotation cylinder. (c) The surface speed ratio between the cylinder ( $a = 30$  mm) and the drum versus rotation frequency of the drum. (d, e) The rotation frequency of the cylinder, for (d)  $a = 30$  mm and (e)  $a = 7.75$  mm, as function of the rotation frequency of the drum, which was varied both in ascending order (red circles) and descending order (blue triangles). The gap between the vertical arrows in (d, e) give an indication of the hysteresis.

### 3. Transition between co-rotation and counter-rotation, regimes of co-rotation and counter-rotation

#### 3.1. Transition between co-rotation and counter-rotation

The cylinder was heavier than the water and sat at the bottom of the drum when it was at rest. When the drum was set into motion at a prescribed rotation rate, the cylinder adapted its rotation frequency and azimuthal position according to the prescribed value and history of the setting of the drum frequency. The general behavior of the cylinder was as follows. At lower  $f_{drum}$  values, it intermittently touched the wall, and rotated in the same direction as the wall of drum. The surface speed of the cylinder was close to that of the wall, i.e. the significant slip which is typical of very viscous flows (Seddon & Mullin (2006)) was not observed here. Beyond a certain threshold frequency, the cylinder lifted from the wall and rotated in a direction which was opposite to that of the drum. The rotation frequency  $f_{cy}$ , the azimuthal position  $\theta$  and the gap width  $G$  between the cylinder and the wall all depended on the drum frequency.

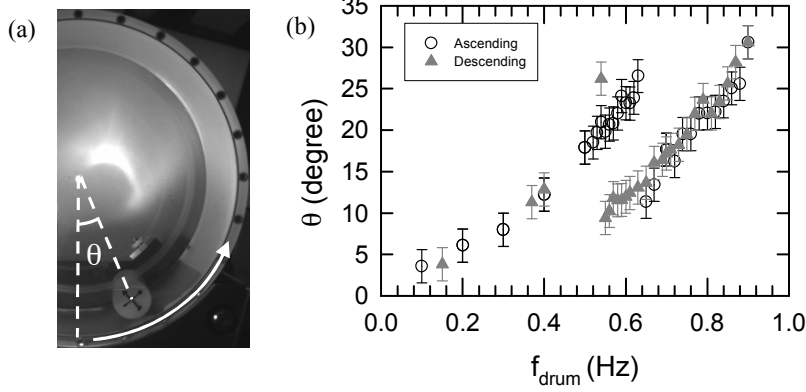


FIGURE 3. (a) Representative frame to demonstrate the measurement of the azimuthal position. (b) The azimuthal position of the cylinder ( $a = 30$  mm) as a function of rotation frequency of the drum, which was varied both in ascending order (red circles) and descending order (blue triangles). The error bars indicate uncertainty caused by the small wiggling motion of the cylinder, which was found to be less than  $\pm 2^\circ$ .

*Cylinder rotation frequency* Plots of the rotation frequency of the cylinder  $f_{cy}$  versus the rotation frequency of the drum  $f_{drum}$ , for cylinders of radii 7.75 and 30 mm, are shown in Fig. 2 (d, e). The data plotted as open circles (triangles) were obtained while increasing (decreasing)  $f_{drum}$ . The dependence of  $f_{cy}$  on  $f_{drum}$  for a cylinder of radius  $a = 30$  mm is shown in Fig 2 (d) where can be seen that the cylinder rotated in same direction as the drum, and  $f_{cy}$  increased with increasing  $f_{drum}$  until a critical value  $f_{drum}^{c1} = 0.64$  Hz was reached. The cylinder suddenly reversed its rotation direction when  $f_{drum}$  exceeded this threshold. Both the sign and the absolute value of  $f_{cy}$  changed abruptly at this transition. The maximum value of  $f_{cy}$  just before the transition was 4.30 Hz for  $f_{drum} = 0.64$  Hz jumping to  $f_{cy} = -1.16$  Hz for  $f_{drum} = 0.65$  Hz. As shown in Fig. 2 (d), beyond the transition the absolute value of  $f_{cy}$  for counter-rotating motion decreases with increasing  $f_{drum}$ . The open triangles in the figure represent  $f_{cy}$  versus  $f_{drum}$  when the experiments were operated with decreasing  $f_{drum}$ . The cylinder counter-rotated with  $f_{cy} = -0.91$  Hz when  $f_{drum}$  started with 0.90 Hz, and the rotation rate decreased to  $f_{cy} = -1.23$  Hz with decreasing  $f_{drum}$  to 0.55 Hz. The cylinder changed to co-rotation when  $f_{drum}$  was set to a smaller value than a second threshold frequency  $f_{drum}^{c2} = 0.55$  Hz, i.e. lower than  $f_{drum}^{c1} = 0.64$  Hz. As shown in the figure, except in the hysteresis transition region, the curves  $f_{cy}$  for increasing and decreasing  $f_{drum}$  lie on top of each other. The data near the transition frequencies were measured with increasing or decreasing  $f_{drum}$  using the same increments, and the measurements were performed after a waiting period of 5 to 10 minutes. Hence, the hysteresis is reported with confidence. Plots of the surface speed ratio, defined as  $V_{cy}/V_{drum} = a f_{cy}/R f_{drum}$ , of the cylinder with radius 30 mm and the drum are shown in Fig 2 (c). The surface speed ratio is very close to 1 for co-rotation, and the absolute value is smaller than 0.5 for counter-rotation. It can be clearly seen that the cylinder rotates more slowly in counter- than in co-rotation with a similar  $f_{drum}$ .

The observed hysteresis was also found for smaller cylinders, though the difference between the two thresholds decreased as radius of the cylinder was reduced. The dependence of  $f_{cy}$  on  $f_{drum}$  for a cylinder with diameter 7.75 mm is shown in Fig. 2 (e). The overall trend of  $f_{cy}$  versus  $f_{drum}$  is similar to that of the cylinder with  $a = 30$  mm. However, the difference between the two transition frequencies,  $f_{drum}^{c1} = 0.19$  Hz and  $f_{drum}^{c2} = 0.18$  Hz, for this cylinder is much smaller than that for the larger cylinder reported

above. The observed hysteresis presumably has its origins in the history of the flow field which is different when the drum goes from low to high rotation frequency compared to the opposite case. We will show later that this is a result of the interaction of the cylinder with its own wake, which is qualitatively different for increasing and decreasing  $f_{drum}$ . The experimental results also indicate that, as expected, the wake of a smaller cylinder is weaker than of a larger cylinder, which is also consistent with the trend for the observed hysteresis. Hysteresis was also reported by Kano & Yagita (2002) in lift force measurements of a rotating circular cylinder near a moving plane wall.

*Azimuthal position of the cylinder* Just as the rotation frequency, the azimuthal position  $\theta$  of the cylinder, shown in Fig. 3 (a), is also a function of the drum rotation frequency  $f_{drum}$ . For the cylinder with  $a = 30$  mm this dependence is shown in Fig. 3 (b). The open circles (triangles) are the measurements made when  $f_{drum}$  was increased (decreased). Hysteresis was also found in the  $\theta$  measurements, and the critical transition frequencies,  $f_{drum}^{c1}$  and  $f_{drum}^{c2}$ , are in accord with those from the frequency measurements discussed above. Apart from the hysteresis regime, the data sets for increasing and decreasing  $f_{drum}$  can again be collapsed, as shown in fig. 3 (b). The angle  $\theta$  increases with  $f_{drum}$  for both co- and counter-rotation. However, the angle  $\theta$  at which co-rotation sets in is larger than that for counter-rotation with the same  $f_{drum}$ , see fig. 3 (b). As in the case of the frequency measurements of  $f_{cy}$ , the hysteresis of  $\theta$  is reduced for the smaller cylinder.

*Gap width* The cylinder was observed to sit very close to the drum wall when it was co-rotating with the drum as shown in fig. 4 (a). In this case, the width of the gap between the cylinder surface and the drum wall was below the resolution of the measurements. Since the pressure force, a detailed account of which is given in Sec. 5.2, is too small to balance the radial component of gravity, a normal force exerted by the wall must support the cylinder. This is confirmed by Fig. 2(c) which shows that the surface speeds of the cylinder are nearly equal to the speed of the drum wall, implying friction dominates. The speed of the cylinder reduces when the drum is close to the transition frequency and the cylinder begins to slip with respect to the wall.

The situation was found to be quite different when the cylinder counter-rotated with the drum. Then the cylinder ‘floated’ above the wall instead of being in contact with it, as can be seen in fig. 4 (b). The measurements of the gap width  $G$  versus  $f_{drum}$  for the counter-rotation cylinder with radius of  $a = 30$  mm are presented in Fig 4 (c). It can be seen that  $G$  is an increasing function of  $f_{drum}$ . The hysteretic behavior is the same for the frequency and angle measurements. The gap width shown in Fig. 4 (c) was estimated using snapshots obtained from the respective experimental condition. However, the cylinder did not always rotate at precisely the same fixed position during the measurements, and a small wiggling motion produced an error. Averaging over many snapshots gave an error estimate of less than 20% in the measurements of the gap and this is indicated by the error bars in the figure.

We separately discuss the observed phenomena for the co- and counter-rotation cases in the following section.

### 3.2. Co-rotation

Prokunin (2003) studied the motion of a rigid particle rolling down an inclined plane in a fluid at low values of  $Re$ . It was found that the particle rolled under its own weight, and exhibited both hydrodynamic slip and contact with the wall. Yang *et al.* (2006) measured the speed ratio of a rough sphere in a rotating drum at low values of  $Re$ . They found that the speed ratio between the sphere and the wall was approximately one when the

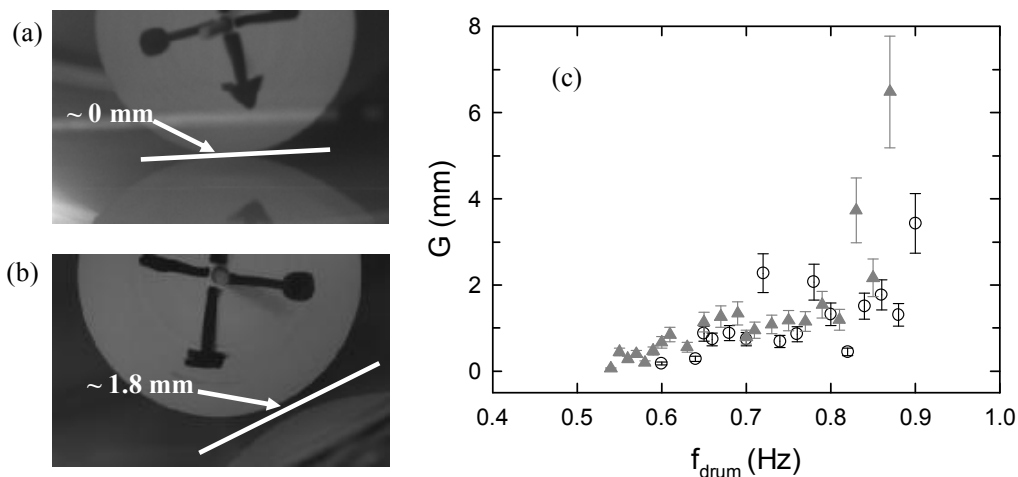


FIGURE 4. The snapshots indicate that (a) the gap thickness for co-rotation case with  $f_{drum} = 0.10$  Hz; (b) the gap thickness for counter-rotation with  $f_{drum} = 0.86$  Hz. The radius of the cylinder is 30 mm, and the solid line marks the wall of the drum. Its curvature is not seen on the scale of this figure. (c) The measured gap width as a function of  $f_{drum}$  for the cylinder of radius 30 mm in the counter-rotation situation. The drum was operated both in ascending mode (red circles) and descending mode (blue triangles). The error bar in (c) is 20% of the gap thickness.

rotation frequency of the drum was low so that the sphere moved with the drum via the frictional contact with the wall. At faster drum rotation the sphere began to slip with respect to the drum wall and smoothly departed from the contact regime.

Not unexpectedly, frictional interaction between the heavy cylinder and the drum forces the former to co-rotate. In the limiting case, the cylinder completely rolls along the drum wall. In this situation, the rotation frequencies of the cylinder and the drum are inversely proportional to their radii, i.e.  $f_{cy}/f_{drum} = R/a$ . The ratio between two rotation frequencies is plotted as a function of  $f_{drum}$  (in the co-rotation case) for a number of different cylinders in Fig. 5. The solid lines depict the ratios between the drum radius and the respective cylinder radii, and hence indicate friction dominates the motion for the different cylinders. Fig. 5 shows that the measured data collapse on these lines, and this indicates that the cylinder indeed moved with the drum (via the frictional contact with the wall). The deviation between the data and the line at higher  $f_{drum}$  suggests that the cylinder then started to slip. The cylinder frequency was much lower than that of the rolling motion when  $f_{drum}$  was close to the critical frequency, where the transition to counter-rotation took place.

### 3.3. Counter-rotation

As discussed above, the cylinder counter-rotated once the drum rotation frequency was larger than a threshold value. In counter-rotation, the cylinder freely rotated without contact with the wall and there was a significant gap between it and the wall. Here we focus on the cylinder rotation frequency, the azimuthal location, and the gap width in the counter-rotation case.

The counter-rotating cylinder self-selected a rotation frequency and an azimuthal location according to the set frequency of the drum and the radius of the cylinder. The relationship between  $f_{cy}$  and  $f_{drum}$  for different cylinders in counter-rotation is shown in Fig. 6 (a). The cylinder counter-rotated with respect to the drum, so that  $f_{cy}$  in the plot

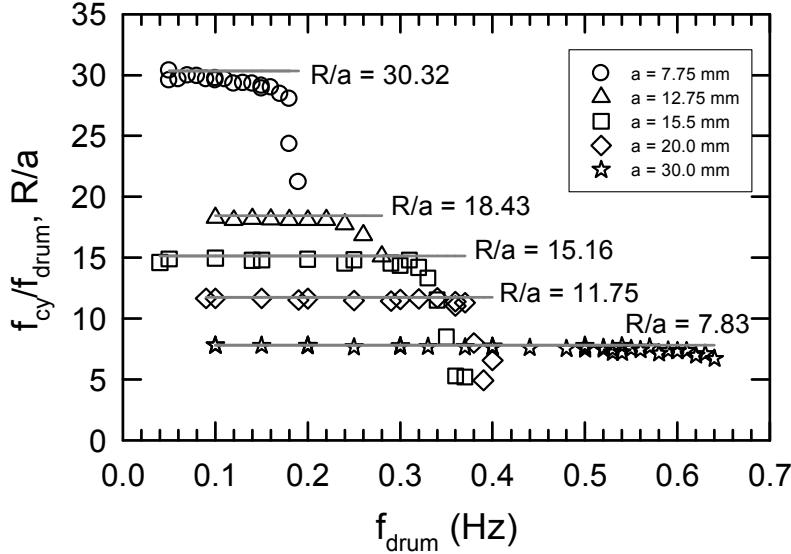


FIGURE 5. Co-rotating case: The ratio between  $f_{cy}$  and  $f_{drum}$  as a function of  $f_{drum}$  for different cylinders. The solid lines represent the ratio of the radii of the drum and the cylinder.

is negative. The absolute value of  $f_{cy}$  decreased approximately linearly with increasing  $f_{drum}$  for all cylinders, the cylinder tended to slow down as the speed of the drum increases, i.e. the opposite to the case of co-rotation. As shown in Fig. 6 (a), the cylinder with  $a = 7.75$  mm began to counter-rotate at 2.1 Hz when  $f_{drum} = 0.2$  Hz, and slowed down to 0.4 Hz when  $f_{drum}$  was 0.4 Hz. Above this frequency the cylinder started to wiggle around instead of rotating steadily at a fixed position. Stewart *et al.* (2006, 2010) studied the wake of a rolling cylinder/sphere along a wall, and they found that the wake becomes unsteady for Reynolds number above a few hundred. In the present studies, the cylinders freely counter-rotated with the drum. We also found that the cylinder motion was no longer stable when the drum frequency was increased further. The transition Reynolds number, from stable rotation to unstable motion, depended on the cylinder radius. Here we only report measurements for stable rotation of the cylinder.

The frequency of  $f_{drum}$  at which counter-rotation was proportional to the diameter of the cylinder and ranged from 0.2 Hz for  $a = 7.75$  mm to 0.55 Hz for  $a = 30$  mm. Each cylinder lost stability to time-dependent motion and started to wiggle when  $f_{drum}$  was larger than the maximum value of  $f_{drum}$  given on the plot. This limiting frequency for stable rotary motion of the cylinder is also proportional to its diameter as can be seen in Fig. 6 (a). It changes from 0.4 Hz for the cylinder of  $a = 7.5$  mm to 0.9 Hz for the  $a = 30$  mm cylinder.

The self-selected azimuthal position  $\theta$  of the cylinder also depends on  $f_{drum}$  as shown in Fig. 6 (b). The cylinder generally rotated stably during the measurements, however, it was never perfectly still and there was always a small amplitude wiggling motion present. This was analyzed in detail for a particular case and the error induced by the wiggling motion was found to be less than  $2^\circ$  as indicated by the error bars marked on the plot. The angle ( $\theta$ ) at which counter-rotation starts increases approximately linearly with  $f_{drum}$  for all cylinders, but has a different slope for each.

The gap between the cylinder and the drum wall was also self-selected by the cylinder for given  $f_{drum}$ . The measured gap width is shown in Fig. 6 (c) plotted as a function of



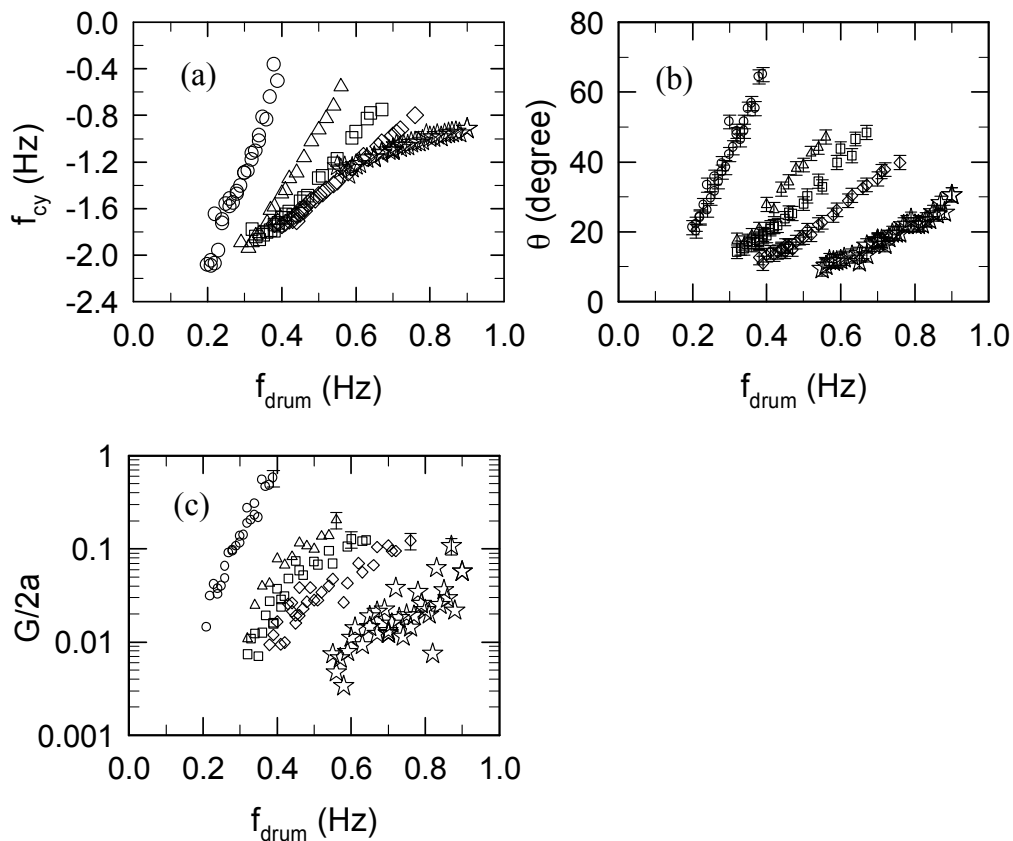


FIGURE 6. Counter-rotating case: The measured (a) cylinder rotation frequency (b) azimuthal position of the cylinder, and (c) the normalized gap width between the cylinder and the drum wall as a function of  $f_{drum}$  for the cylinders of different radii. The measurement error bar shown in (b) is  $\pm 2^\circ$ . The error bar in (c) is 20% of the gap thickness, only maximum error bar for each cylinder is shown. The symbols are same with Fig. 5; Open circles:  $a = 7.75$  mm, open triangles:  $a = 12.75$  mm, open squares:  $a = 15.5$  mm, open diamonds:  $a = 20.0$  mm, open stars:  $a = 30.0$  mm.

$f_{drum}$  for each individual cylinder when in counter-rotating. The data clearly indicate that the gap width is an increasing function of  $f_{drum}$  and for fixed  $f_{drum}$ , a larger gap was found for smaller cylinders. It is quite remarkable that the gap is of the order of a millimeter, which is significantly larger than the micrometer range found by Seddon & Mullin (2006) in the Stokes flow regime. The maximum gap width in this case was several millimeters and this allowed us to visualize the flow around the cylinder using particle image velocimetry (PIV).

The dependence of the rotation frequency  $f_{cy}$  on its azimuthal location  $\theta$  and the gap thickness  $G$  presented in this section will all be used to derive the drag and lift coefficients discussed in Sec. 5.

#### 4. Velocity measurement

The flow field around the cylinder determines the forces exerted on it. Particle Image Velocimetry (PIV) was employed to study the flow around the cylinder in the  $x-z$  plane, see Fig. 1, for both co- and counter-rotation situations.

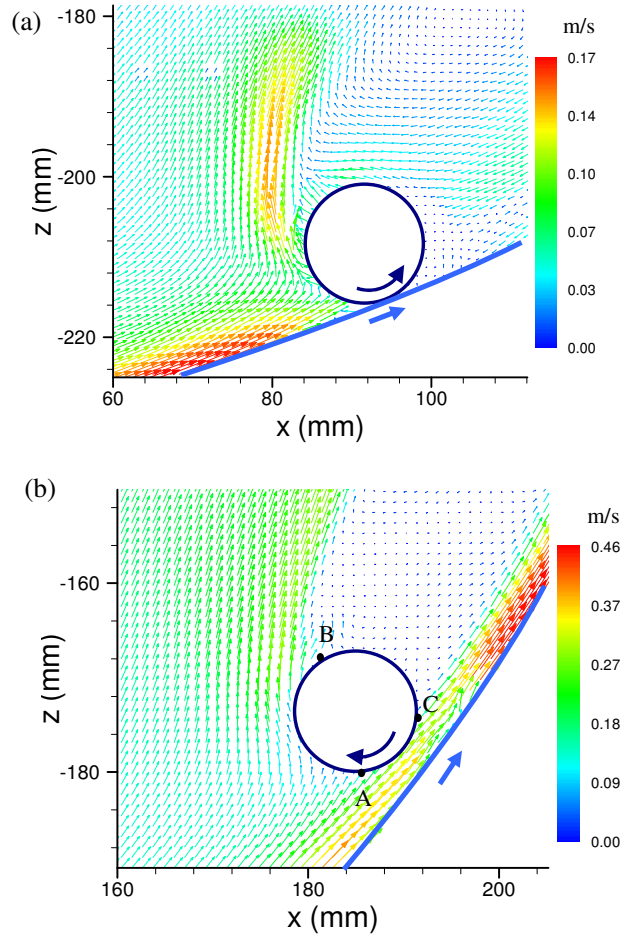


FIGURE 7. The measured time-averaged velocity around the cylinder with radius  $a = 7.75$  mm. The velocity maps were averaged with 300 instantaneous velocity snapshots with a frequency of 50 Hz. The magnitude of the velocity  $(U^2 + W^2)^{1/2}$  was coded in color scale in units of m/s. (a) The cylinder co-rotates with the drum with the set frequency  $f_{drum} = 0.15$  Hz. (b) The cylinder counter-rotates with the drum operating at  $f_{drum} = 0.35$  Hz. Supplementary movies (movie 3 and movie 4) show the time evolution of the instantaneous velocity maps.

#### 4.1. Visualization of local flow around cylinder

The time-averaged velocity map around the co-rotating cylinder with radius 7.75 mm is shown in Fig. 7 (a). The rotating frequency of the drum was set to  $f_{drum} = 0.15$  Hz, and the cylinder was co-rotating with a frequency of 4.33 Hz; the azimuthal position was  $\theta = 23.5^\circ$ . The ratio between the two rotation frequencies is  $f_{cy}/f_{drum} = 28.87$ , which is slightly smaller than the radii ratio  $R/a = 30.32$ . This suggests that the cylinder did not completely roll along the wall of the drum, and there was some slipping motion between the cylinder and the wall. As shown in Fig. 7 (a), the flow cannot pass between the cylinder and the wall and this induces a strong upward flow. Associated with this upward flow is a shear stress exerted on the cylinder. With increasing frequency of the drum the couple on the cylinder become larger and eventually overcomes the forcing from the wall and the cylinder starts to rotate in a sense opposite to the drum.

As soon as the cylinder starts to counter-rotate, a gap develops between the cylinder

and the wall. The time-averaged velocity map around the cylinder for the counter-rotating case is shown in Fig. 7 (b). The cylinder was lifted above the wall, reaching a distance of about 3.3 mm. As shown in Fig. 7 (b), in this case, the maximum velocity is close to the wall, i.e. inside the gap and hence the primary route for the mass flux is through the gap. The small difference is within the measurement error. The mass flux coming from upstream must be transferred to downstream through the gap. The flow velocity inside the gap is quite close to the upstream flow velocity, and the small difference may be induced by measurement error. Beyond the separation point, the acceleration is caused by the interaction between dividing streamline and the wake.

When a cylinder moves in a *uniform* flow far from a wall and without rotatory motion, the separation points are located *symmetrically* with respect to a line joining the forward separation point with the center of the cylinder. In the present case of the counter-rotating cylinder, the separation points are *not* symmetric. The boundary layer on the cylinder cannot be resolved using PIV. However, an estimate of the location of the stagnation point can be made using the information on the flow direction adjacent to the cylinder surface. As shown in Fig. 7 (b), the separation point (C) is located near the position where high velocities exist in the gap. The counter-rotation motion and the vicinity of the wall forces the separation point (B) to move downstream and the stagnation point (A) to move towards the wall. Hence the location of the stagnation and separation points imply that the tangential shear stress on the surface between the point A and C is larger than that between A and B. The overall tangential shear stress on the surface of the cylinder therefore drives the counter-rotation of the cylinder. The lift force acting on the counter-rotating cylinder acts to balance forces resulting from the normal component of gravity and inertial pressure force. The movement of the separation points for a cylinder near a wall were also studied in experiments by Labraga *et al.* (2007), who found a similar trend. As we will show later, a large lift coefficient on the cylinder can be obtained and this arises principally because the nearby wall.

The PIV velocity measurements were conducted under different experimental conditions to quantify the flow field in the drum. The measurements were performed in the central ( $x - z$  plane at  $y = 0$ ) as shown in Fig. 1. The time-averaged velocity maps presented in the following section were obtained by averaging 50 to 300 instantaneous velocity frames which were captured with a measurement frequency of 50 Hz. It was found that 50 velocity frames are sufficient to achieve a convergent time-averaged velocity map.

#### 4.2. The velocity field without cylinder

A check was first performed to establish whether the flow in the drum without a cylinder was in solid-body rotation. Bluemink *et al.* (2008) estimated the spin-up time to achieve solid-body rotation starting from rest is approximately 4 minutes for water. All data in the present measurements were taken after this waiting period.

As a check, it was decided to measure the flow field directly. The time-averaged velocity field measured in the  $x - z$  plane of the drum operated at a rotation frequency of  $f_{drum} = 0.40$  Hz is shown in Fig. 8 (a). Practical limitations of the laser light intensity meant that only the central part of the vertical direction was measured. The selected measurement area was  $470 \text{ mm} \times 196 \text{ mm}$ , which corresponds to  $-R$  to  $R$  in  $x$  direction and  $-0.42R$  to  $0.42R$  in  $z$  direction. The spatial resolution between two vector arrows was  $5.93 \text{ mm}$  in both  $x$  and  $z$  directions. A profile of the vertical velocity along the  $x$ -axis, extracted from the measured velocity map in  $z = 0$ , is plotted in figure 8 (b). The vertical velocity depends linearly on the horizontal position  $x$ , confirming solid-body rotation. The rota-

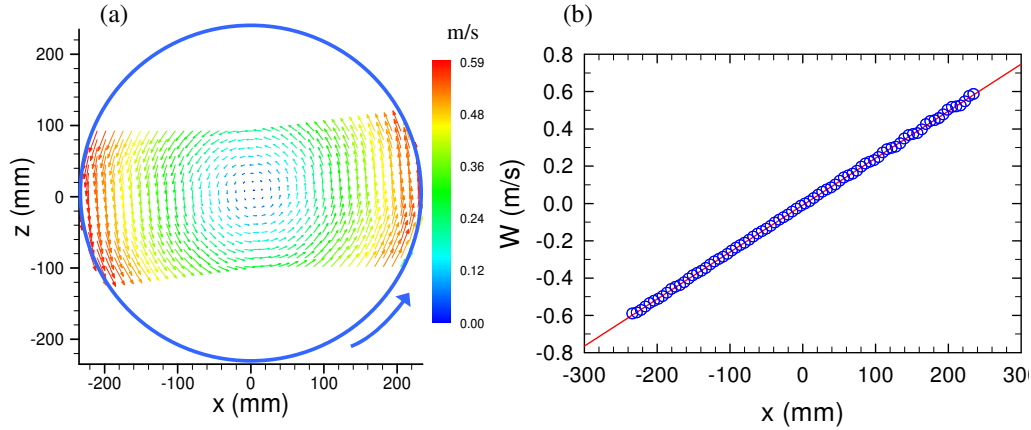


FIGURE 8. (a) The time-averaged velocity vector map, in the drum without a cylinder, measured with the set frequency  $f_{drum} = 0.40$  Hz. For better readability, a coarse-grained map is shown here with only  $1/4$  of the measurement arrow density. The magnitude of the velocity was coded in color scale in m/s. The time average was taken over a period of 6 seconds corresponding to 300 velocity frames. (b) The horizontal profile of the vertical velocity  $W$  extracted from the measured velocity maps in (a). The straight line corresponds to the fitting result ( $f_{drum} = 0.401$  Hz), which is very close to solid-body rotation.

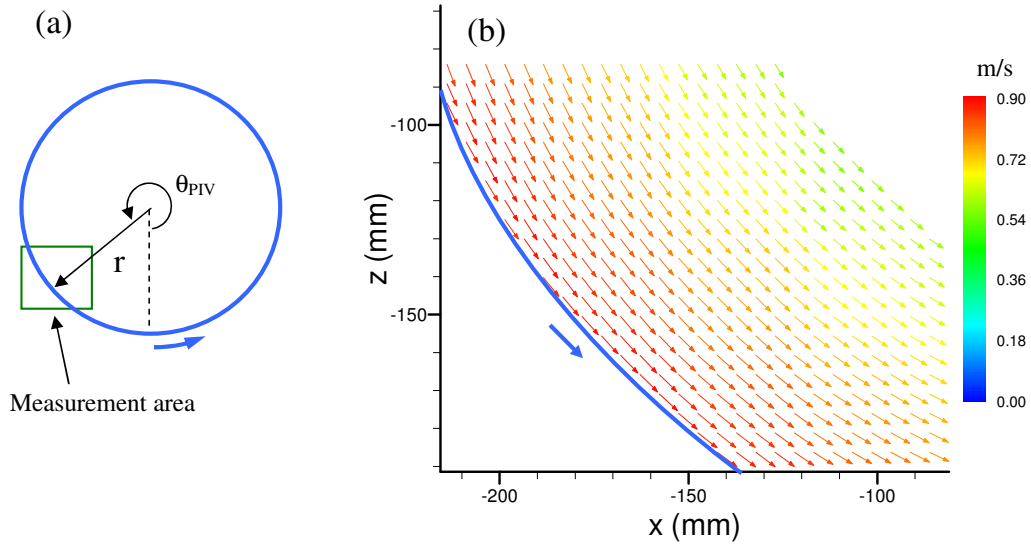


FIGURE 9. (a) A sketch of the measurement area for the high resolution PIV measurement. The angular location of the measurement center is  $\theta_{PIV} = 256.8^\circ$ . (b) The time-averaged velocity vector map measured at  $f_{drum} = 0.60$  Hz. For better readability, a coarse-grained map is shown here with only  $1/9$  of the measurement arrow density. The magnitude of the velocity was coded in color scale in m/s. The time average was taken over a period of 6 seconds, corresponding to 300 velocity frames.

tion frequency for the drum based on the measured slope is 0.401 Hz, which is very close to the set value of 0.40 Hz.

To study the flow velocity near the wall of the drum in detail, higher resolution PIV measurements were performed in this region for frequencies from 0.10 to 0.90 Hz. The measurement area was  $134 \text{ mm} \times 107 \text{ mm}$ , which offered us a spatial resolution 1.7

mm between two vector arrows. A sketch of the measurement location is shown in Fig. 9 (a) where the angular location of the measurement center was  $\theta_{PIV} = 256.8^\circ$ . The time-averaged velocity vector map measured with a drum rotating frequency of 0.60 Hz is shown in Fig. 9 (b). A coarse-grained velocity map is reproduced here with only 1/9 of the measurement arrow density to enable a printable figure. The magnitude of the velocity was coded in color scale in units of m/s. In fact, the magnitude of the velocity was found to be almost identical with the value of the tangential velocity  $V_\theta$  because the flow is in almost perfect solid-body rotation. The standard derivations for horizontal and vertical velocity components, averaged in the whole map, were found to be only 0.025 m/s, which is far smaller than the mean flow velocity. This suggests that the flow is stationary.

#### 4.3. The velocity field with an inserted cylinder in the drum

Solid-body rotation was disturbed when a cylinder was placed in the drum. We will now quantify this effect through PIV measurements and will, in particular, clarify whether the flow field returns to solid-body rotation after traveling a certain distance downstream the cylinder.

Firstly, the evolution of the flow velocity behind the cylinder was studied by measuring the velocity distributions at different azimuthal positions. A sketch of the cylinder location and the PIV measurement positions in the drum is shown in Fig. 10 (a). The radius of the cylinder was 30 mm in this measurement. The cylinder counter-rotated with  $f_{cy} = -4.4$  Hz when the drum rotation frequency was set to  $f_{drum} = 0.60$  Hz. The gap between the cylinder and the wall was approximately 0.2 mm, and the respective azimuthal location of the cylinder center was  $\theta = 12 \pm 2^\circ$ . High resolution PIV measurements were performed to measure the flow field at different distances from the cylinder. These were made at four different azimuthal positions with  $\theta_{PIV} = 48^\circ$  (P1),  $122^\circ$  (P2),  $239^\circ$  (P3), and  $312^\circ$  (P4), respectively. The respective distances traveled by the wake normalized by the cylinder diameter, i.e.  $(\theta_{PIV} - \theta)(R - a)/2a$ , were 2.1, 6.5, 13.5, and 17.9, with  $\theta$  expressed in radians.

The time-averaged velocity maps at the measurement areas P1, P2, P3, and P4 are presented in Figures 10 (e, c, b, d), respectively. The color code for the velocity is the same as that in Fig. 9 (b), since the experiments were carried out at the same drum rotation frequency. At  $f_{drum} = 0.60$  Hz the maximum velocity is 0.90 m/s for a drum without a cylinder, as shown in Fig. 9 (b). However, the maximum flow velocity, at the same  $f_{drum}$ , for all four positions is only around 0.4 m/s, which is significantly smaller. The measurement area P1 measures the velocity field just downstream the cylinder, the wake generated by the cylinder is clearly visible in Fig. 10 (e). The flow certainly develops with increasing distance from the cylinder. The vortex disappears in the measurement area P2, and some vectors tend to align in tangential direction. However, a significant number of vectors do not point in the tangential direction, especially in the lower part, as shown in Fig. 10 (c). The flow continues to develop with increasing distance from the cylinder. As shown in 10 (b, d), almost all velocity vectors in the velocity maps measured at P3 and P4 point in tangential direction. Moreover, the velocity patterns in measurement areas P3 and P4 are very similar as shown in Fig. 10 (b, d). This suggests that the flow has achieved a steady state at the measurement area P3 and P4. However, it is far from the solid-body rotation without a cylinder, as shown by the clear difference of the velocity patterns and the velocity magnitudes between Fig. 9 (b) and Fig. 10 (d).

In order to compare the velocity profiles quantitatively, the tangential velocity  $V_\theta(r)$  plotted as a function of the radial distance from the drum center ( $r$ ) at each measurement position is shown in Fig. 11. The radial profile was obtained by averaging the velocity

vectors with the same  $r$ , with angle between  $\theta_{PIV} - 2.5^\circ$  and  $\theta_{PIV} + 2.5^\circ$  in each of the measurement areas. For comparison, the velocity profile in the drum without a cylinder, extracted from Fig. 9 (b), is also shown plotted in the figure using open circles. The profile for solid-body rotation with the same  $f_{drum}$  is also shown in the plot (solid line). As shown in Fig. 11, again the velocity profile in the drum without cylinder agrees with the solid-body rotation. However, all the profiles, with the cylinder at four positions, do not follow solid-body rotation in either the magnitude of the velocities or the shape of the profiles. The velocity profile at P1 is clearly disturbed significantly by the cylinder. It develops with distance from the cylinder, and the velocity profiles at P3 and P4 are almost identical. This suggests that the flow at P3 (and P4) is already in a stationary stable state, since it does not change with increasing distance from the cylinder. This well developed velocity profile at measurement position P4 corresponds to the incoming velocity profile for the cylinder. The profile is not linear, as it would be for solid-body rotation, but is instead curved. The velocity rapidly decreases at a short distance from the wall, and it changes slowly with further increase of the distance from the wall, as shown in Fig. 11.

#### 4.4. The incoming velocity

As discussed above, the incoming velocity  $V_0$  to the cylinder does not correspond to solid-body rotation. In order to quantify the effect of this, velocity fields were measured at the position P4 for various cylinders at different drum frequencies. Since we focus on the force measurements on a counter-rotation cylinder, the measurements were only performed in the counter-rotation regime. The results for the tangential velocity are presented in Fig. 12. The cylinder with radius  $a = 30$  mm counter-rotated with the drum over the frequency range used here. The profile shapes are similar, and, as expected higher velocities were found for higher  $f_{drum}$ . For the various cylinders and various  $f_{drum}$  the radial velocity profiles  $V_\theta(r)$  at P4 were determined. Those for  $a = 30$  mm are shown in Fig. 12. As discussed previously, the gap between the cylinder and the wall of the drum is very small. We neglect this for the calculations of the incoming velocity.

With measured tangential velocity  $V_\theta(r)$  and cylinder radius  $a$ , we define the incoming velocity  $V_0$  as the average of the tangential velocity between  $R$  and  $(R-2a)$ ,

$$V_0 = \frac{1}{2a} \int_R^{R-2a} V_\theta(r) dr. \quad (4.1)$$

The incoming velocity based on a solid-body rotation is  $2\pi f_{drum}(R-a)$ . The ratio between the measured incoming velocity  $V_0$  and the one based on a solid-body rotation measures the degree of the perturbation by the cylinder. This ratio is defined by

$$\beta = \frac{V_0}{2\pi f_{drum}(R-a)}. \quad (4.2)$$

We measured the ratio for every cylinder under several frequencies in its parameter range, as shown in Fig. 13. The data indicates that  $\beta$  is roughly constant for a given cylinder radius  $a$  in the measured parameter regime and becomes smaller for larger cylinders. Averaged over various  $f_{drum}$  values of the ratios  $\beta$  are  $\bar{\beta}(a) = 0.48, 0.41, 0.41, 0.35$  and  $0.32$  for the cylinders with the radius of  $a = 7.75, 12.75, 15.5, 20$  and  $30$  mm respectively. It was impractical to measure and calculate the ratio  $\beta$  for all frequencies for all of the cylinders. Since the value of  $\beta$  only depends weakly on  $f_{drum}$  for a given cylinder,  $\bar{\beta}(a)$  offers us a way to translate the velocity based solid-body rotation to the incoming velocity. For the remainder of the paper, we will use these measured averaged ratio  $\bar{\beta}(a)$  to translate the incoming velocities  $V_{in}$  from a solid-body flow, for different

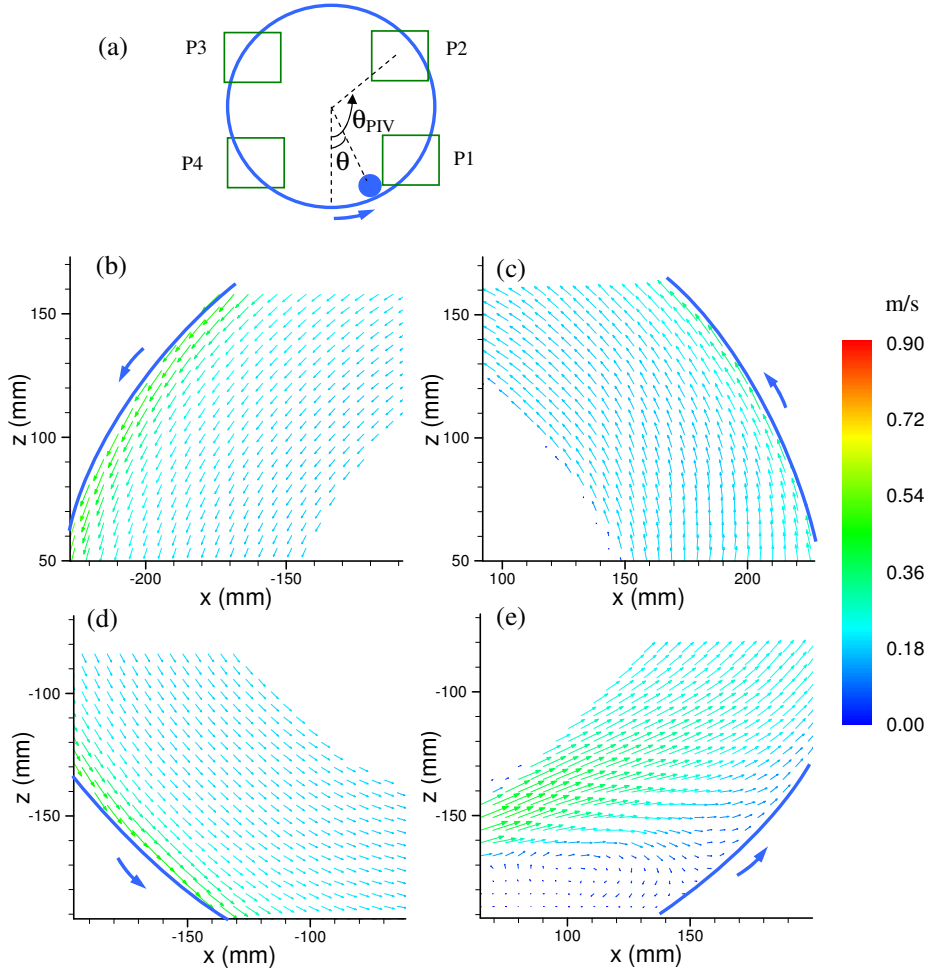


FIGURE 10. (a) A sketch of the cylinder location and the PIV measurement positions in the drum. The radius of the cylinder was 30 mm in this measurement and the set drum rotating frequency was  $f_{drum} = 0.60$  Hz. (b-e) The time-averaged velocity maps measured at P3, P2, P4 and P1. For the sake of clarity, the coarse-grained maps are shown here with only 1/9 of the measurement arrow density. The magnitude of the velocity was coded with the same color scale as that in Fig. 9 (b) with the same set frequency. The time average was taken over a period of 1 seconds corresponding to 50 velocity frames.

rotation frequencies  $f_{drum}$  and radius of the cylinder  $a$  as

$$V_{in}(f_{drum}, a) = \bar{\beta}(a)[2\pi f_{drum}(R - a)] \quad (4.3)$$

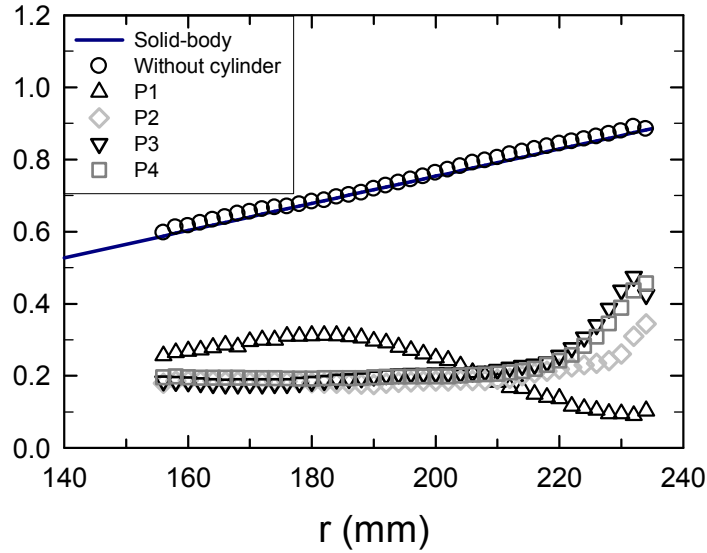


FIGURE 11. The tangential velocity  $V_{\theta}(r)$  versus the radial distance at different measurement positions. The drum rotation frequency is  $f_{drum} = 0.60$  Hz and  $a = 30$  mm. The respective velocity profile, with the same  $f_{drum}$ , in the drum without cylinder is plotted with open circles and that for a solid-body rotation is shown as solid line. A considerable velocity reduction is seen throughout.

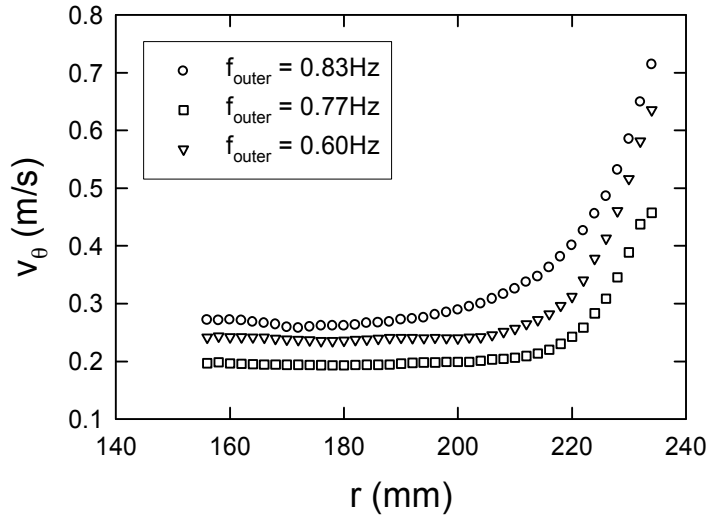


FIGURE 12. The tangential velocity profiles versus the radial distance measured at the measurement position 4 for various set frequencies. The cylinder inside the drum has an radius of 30 mm.



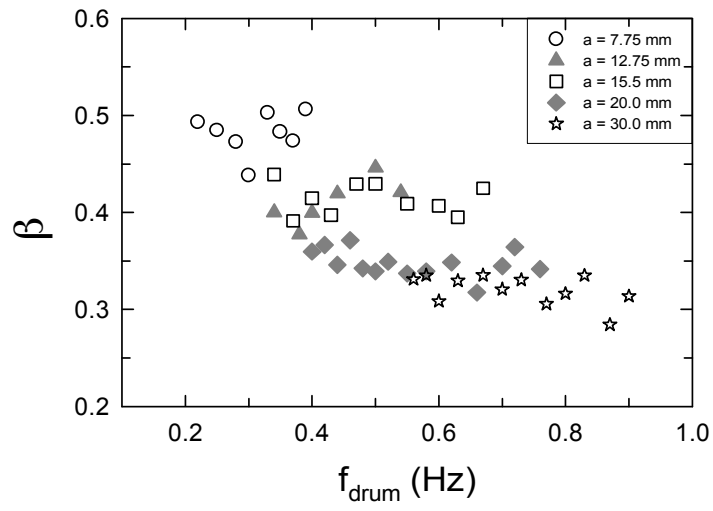


FIGURE 13. The normalized incoming velocity plotted as a function of the drum frequency for different diameter cylinders.

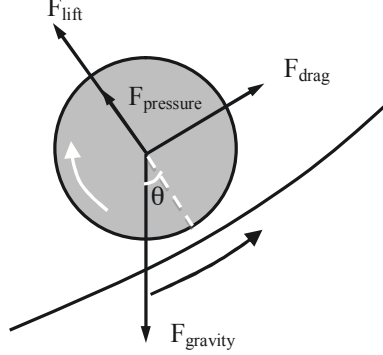


FIGURE 14. Balance between gravity, centrifugal force, drag, and lift force. The inner cylinder counter-rotates as compared to the drum.

## 5. Drag and lift coefficients

### 5.1. Balance of the forces

We define three dimensionless numbers, the Reynolds number  $Re = \frac{V_{in}d}{\nu}$ , the non-dimensional rotation rate  $\alpha = \frac{2\pi f_{cy}a}{V_{in}}$ , and the gap to diameter ratio  $G/2a$ . Here  $\nu$  is kinematic the viscosity of the water. The forces exerted on the small cylinder, per unit length, are the gravity (including buoyancy)  $\mathbf{F}_{gravity}$ , the drag  $\mathbf{F}_{drag}$  and the lift  $\mathbf{F}_{lift}$ . In addition, there is a pressure force  $\mathbf{F}_{pressure}$ , which results from the rotation of the fluid in the drum. In the absence of the small cylinder it causes a pressure field  $p_{fluid} = const. + \frac{1}{2}\rho_f(2\pi f_{drum}r)^2$ . The force on the small cylinder is

$$-\int_{A_{cy}} p_{fluid} \mathbf{n} dA = -\int_{volume} \nabla p dB \quad (5.1)$$

where  $dA$  and  $dB$  are surface and volume elements of the small cylinder, respectively, and  $\mathbf{n}$  is the outward normal to the small cylinder. Since the radii  $a$  of the employed cylinders are all small with respect to the drum radius  $R$  (typically  $a/R$  is about 5%), we may take  $\nabla p$  in Eqn. 5.1 as constant over the cylinder and equal to  $-\rho_{fluid}V_{cy}^2/(R-a)\mathbf{e}_r$ , where  $\mathbf{e}_r$  is a unit vector in radial direction in the drum. There is a further inertia force in radial direction due to change of impulse  $-\pi a^2\rho_{fluid}V_{in}$ . This has the value of the expression on the right hand side of Eqn. 5.1 multiplied with the added mass coefficient  $C_A$ , which equals 1 for a cylinder. Hence

$$\mathbf{F}_{pressure} = -(1 + C_A)\pi a^2\rho_{fluid}V_{in}^2/(R - a)\mathbf{e}_r. \quad (5.2)$$

With  $\mathbf{g}$  denoting the acceleration of gravity, including the buoyancy, we have

$$\mathbf{F}_{gravity} = \pi a^2(\rho_{cy} - \rho_{fluid})\mathbf{g}. \quad (5.3)$$

Comparing the right hand sides of Eqn. 5.2 and Eqn. 5.3 in the radial  $\mathbf{e}_r$  direction with each other, and referring to Eqn. 4.3, we see that

$$\frac{F_{pressure}}{F_{gravity}\cos(\theta)} = \frac{\rho_{fluid}}{\rho_{cy} - \rho_{fluid}} \frac{(2\pi\bar{\beta}f_{drum})^2(R - a)}{g\cos(\theta)} (1 + C_A). \quad (5.4)$$

For example, for the cylinder with  $a = 30$  mm, with  $\rho_{cy} = 1400$  and  $\rho_{fluid} = 1000$  kg/m<sup>3</sup> respectively,  $f_{drum} = 0.60$  Hz,  $\bar{\beta} = 0.32$ , and  $\theta = 12^\circ$ , the force ratio (Eqn. 5.4)

equals 0.17. For a fixed cylinder, the ratio increases with increasing drum frequency as  $\theta$  becomes larger. The value of this ratio for this cylinder ( $a = 30$  mm) increases to 0.4 for the maximum operation drum frequency of 0.90 Hz. Typically, this value is reduced for smaller cylinders where the operational frequency range of the drum is also lower. The calculations based on Eqn. 5.4 show that the force ratio changes from 0.04 to 0.45 for all cylinders and measured rotation frequencies. This suggests that the pressure force resulting from rotation is at most one half of the effects of the component of gravity in the radial direction.

The drag force is best represented by the dimensionless drag coefficient  $C_D$  defined as

$$C_D = \frac{F_{drag}}{2a\frac{1}{2}\rho_{fluid}V_{in}^2}. \quad (5.5)$$

From the force balance in the tangential direction (the  $\theta$  direction in Figure 14), it follows that

$$F_{drag} = F_{gravity}\sin(\theta). \quad (5.6)$$

The force balance in the radial direction is more complicated. The general expression for the force balance on a small particle with velocity  $\mathbf{u}$ , say, in a flow with local velocity  $\mathbf{V}$  is, e.g. Magnaudet & Eames (2000),

$$\begin{aligned} \pi a^2 \rho_{cy} \frac{d\mathbf{u}}{dt} = & \left[ C_A \rho_{fluid} \left( \frac{D}{Dt} \mathbf{V} - \frac{d}{dt} \mathbf{u} \right) + \rho_{fluid} \frac{D}{Dt} \mathbf{V} \right] \pi a^2 \\ & + \rho_{fluid} \pi a^2 C'_L (\mathbf{V} - \mathbf{u}) \times (\nabla \times \mathbf{V}) + \mathbf{F}_{gravity} + \mathbf{F}_{drag}. \end{aligned} \quad (5.7)$$

In this expression  $t$  is time and  $d/dt$  and  $D/Dt$  are material derivatives going with the body and the fluid respectively. In our case  $\mathbf{u} = 0$ . In the sum of the first and the second term on the right hand side of Eqn. 5.7, we recognize the pressure force expression in Eqn. 5.2. The lift is defined in Eqn. 5.7 as the part of the radial force solely due to the local vorticity, that is separated from the radial force due to inertia.

The force balance in radial direction gives

$$\mathbf{F}_{lift} = (\mathbf{F}_{gravity} + \mathbf{F}_{pressure})\mathbf{e}_r = -(F_{gravity}\cos(\theta) - F_{pressure})\mathbf{e}_r. \quad (5.8)$$

The lift forces points to the  $-\mathbf{e}_r$  direction. Normally, in this problem, the way of normalizing the lift is by the quantity in the nominator of the expression on the right hand side of Eqn. 5.5, and we only take the absolute value of  $C_L$

$$C_L = \frac{F_{lift}}{2a(\frac{1}{2}\rho V_{in}^2)} = \frac{(F_{gravity}\cos(\theta) - F_{pressure})}{2a(\frac{1}{2}\rho V_{in}^2)}. \quad (5.9)$$

The rotation frequencies of the cylinder  $f_{cy}$  and the azimuthal angles  $\theta$  for all drum frequencies of the individual cylinders were already defined in Fig. 6. When substituting Eqns. 5.2 and 5.3 into Eqns. 5.6 and 5.9, the drag coefficients  $C_D$  and lift coefficients  $C_L$ , directly follow from the experimental measurements.

## 5.2. Drag coefficient

The measured drag coefficient plotted as a function of  $Re$  is shown in Fig. 15 (a). The error bar in the plot is based on the error in the angle measurements, which were estimated to be less than  $\pm 2^\circ$  as shown in Fig. 6 (b). For the sake of clarity, only the maximum error bar for each cylinder is plotted in the figure. The measured coefficients  $C_D$  for the

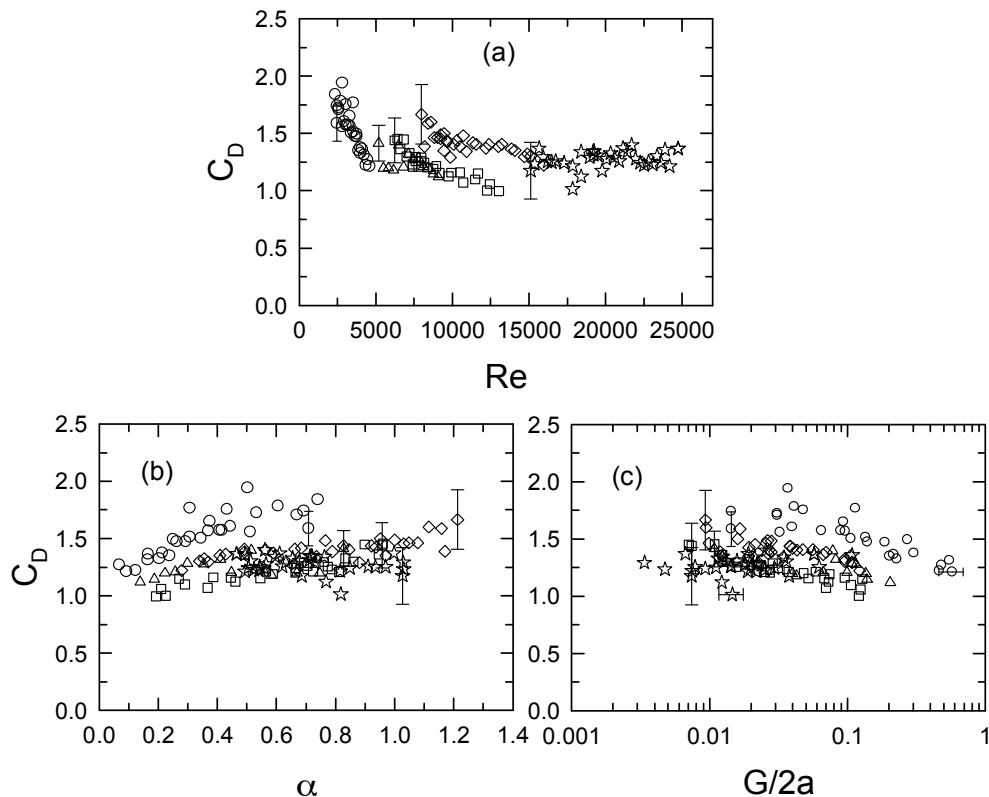


FIGURE 15. The measured drag coefficients for all cylinders versus (a) Reynolds number  $Re$ ; (b) dimensionless rotation rate  $\alpha$ ; (c) the normalized gap width  $G/2a$ . The symbols are the same as those in Fig. 13 for various cylinders with radius  $a = 7.75$  mm (open circles); 12.75 mm (triangles); 15.5 mm (squares); 20 mm (diamonds) and 30 mm (stars). The error bar of the  $C_D$  was calculated based on the error of the angle in the measurements ( $\pm 2^\circ$ ). The horizontal error bar in (c) results from the measurement error in the gap width (20%). For increasing readability, only maximum error bar for each cylinder is plotted.

different cylinders at the same value of  $Re$  collapse reasonably well whereas the measured value  $C_D$  depends weakly on  $Re$ . It is approximately 1.7 for  $Re \sim 2500$  and decreases to approximately 1.2 when  $Re$  increases to 5,000. For even larger values of  $Re$  up to 25,000 the drag coefficient remains close to  $C_D \simeq 1.2$ . The measured values are in good accord with classic measurements on a cylinder in uniform flow (see for example, Goldstein 1965; Clift *et al.* 1978).

When plotting the measured drag coefficient  $C_D$  as a function of the parameter  $\alpha$ , we found it to be nearly independent of  $\alpha$  for all cylinders, except a small increasing trend for the cylinder of  $a = 7.75$  mm. Takayama & Aoki (2004) measured  $C_D$  as a function of  $\alpha$  for  $Re \sim 10^5$ . They found that  $C_D$  decreases with increasing  $\alpha$ . We did not find this trend.

It is known that the onset and cessation of vortex shedding in the flow around a cylinder is affected by placing a wall near the cylinder (Jeffrey & Onishi 1981; Cliffe & Tavener 2004). The characteristics of the flow are determined by  $Re$  and the gap ratio  $G/2a$ , which is the ratio of the the gap distance ( $G$ ) and the cylinder diameter ( $2a$ ) (Nishino *et al.* 2007). Nishino *et al.* (2007) measured the drag coefficient as a function of the gap

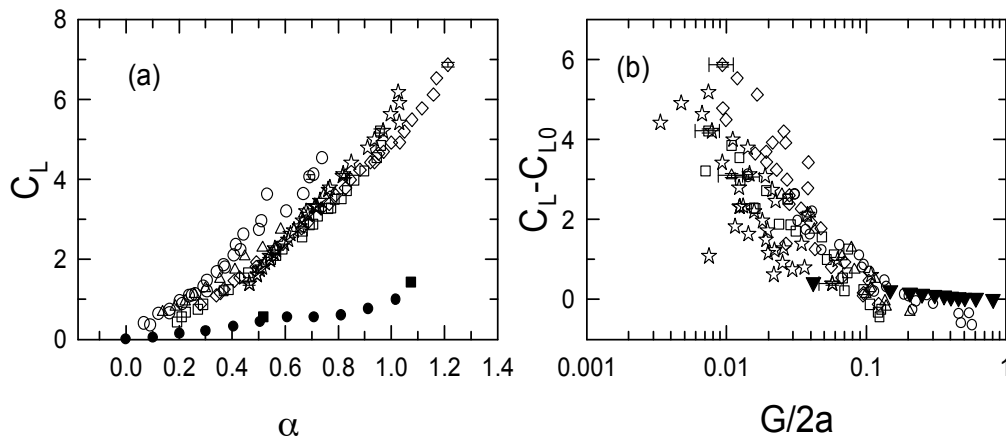


FIGURE 16. (a) The measured lift coefficient  $C_L$  defined by Eq. (5.9) versus the dimensionless rotation rate  $\alpha$ . Solid squares are data from Tokumaru & Dimotakis (1993) of  $Re = 3.8 \times 10^3$ ; solid circles are data of Takayama & Aoki (2004) of  $Re = 4 \times 10^4$ . (b) The corrected lift force by eliminating shear effect  $C_{L0}$  versus the normalized gap thickness  $G/2a$ . Solid triangles are data of Nishino *et al.* (2007) of  $Re = 10^5$ . The open symbols are the same as those in Fig. 13 for various cylinders with radius  $a = 7.75$  mm (open circles); 12.75 mm (triangles); 15.5 mm (squares); 20 mm (diamonds) and 30 mm (stars). The error bar of the  $C_L$  was calculated based on the error of the angle in the measurements ( $\pm 2^\circ$ ). The horizontal error bar in (c) results from the measurement error of the gap width (20%). Only the maximum error bar is plotted for each cylinder for the sake of clarity.

ratio for a cylinder. They found that the drag coefficient gradually decreases as the gap ratio increased, but the dependence is weak. The  $G/2a$  dependence of  $C_D$  for all cylinders used here is given in Fig. 15 (c). Since many experiments were performed with very small gap ratio, the horizontal axis is plotted on a logarithmic scale. The measured  $C_D$  depends weakly on  $G/2a$ , and  $C_D$  decreases slightly with increasing  $G/2a$  when  $G/2a \gtrsim 0.05$ . The measured trend of  $C_D$  versus  $G/2a$ , which is consistent with the results of Nishino *et al.* (2007), shows that the drag coefficient is insensitive to the nearby wall in the present experiments.

### 5.3. Lift coefficient

The measured values of the lift coefficient  $C_L$ , as defined by Eq. (5.9), are plotted versus  $\alpha$  for the various cylinders in Fig. 16 (a). An increasing value of  $C_L$  with increasing  $\alpha$  is revealed for all cylinders. The measured coefficients for different cylinders collapse. The lift coefficient of a cylinder in a uniform flow, with the same definition as  $C_L$ , as measured by Tokumaru & Dimotakis (1993) (solid squares in Fig. 16 (a)), changes from 0 to around 1.5 when  $\alpha$  increases from 0 to 1. Takayama & Aoki (2004) reported a  $C_L$  increasing from 0 to 1 with varying  $\alpha$  from 0 to 1, which is shown with solid circles in Fig. 16 (a).

In the present measurements the value of the  $C_L$  increases from 0 for  $\alpha = 0$  to around 8 for  $\alpha$  around 1.2. The lift coefficient measured in the present experiments is therefore much larger than that in the measurements of Tokumaru & Dimotakis (1993) and Takayama & Aoki (2004) for a rotating cylinder in a uniform flow with similar Reynolds numbers. Tokumaru & Dimotakis (1993) and Takayama & Aoki (2004) showed that the rotational motion indeed offers a way to generate a larger lift coefficient. However, the significant increase of the lift coefficient in the present work is certainly not caused by the rotation of the cylinder alone.

The lift force on a cylinder next to a wall may change significantly as a result of the onset and cessation of the vortex shedding caused by a nearby wall (Nishino *et al.* 2007). Zdravkovich (1985) found that the lift coefficient is governed by the gap to diameter ratio for a cylinder near a plane wall. Nishino *et al.* (2007) found a rapid increase of the lift coefficient as the gap to diameter ratio decreases to less than about 0.5.

Apart from the presence of the nearby wall of the drum, there will certainly be a contribution of the shear in the incoming flow. Recent results, from Sumner & Akosile (2003); Cao & Tamura (2008), for the forces on a cylinder in a shear flow, showed that there is a lift force pointing from the high velocity side towards the low velocity side resulting from the asymmetrical distribution of pressure around the cylinder. In our case this implies a lift force directed towards the low velocity side. According to Sumner & Akosile (2003) and Cao & Tamura (2008), the lift force induced by shear effect depends on the Reynolds number and on the shear rate,  $K$ , defined as

$$K = \frac{2a}{V_{in}} \frac{dV}{dr} \quad (5.10)$$

The Reynolds number in Sumner & Akosile (2003) and Cao & Tamura (2008) are of the same order of magnitude as ours,  $10^3 - 10^4$ . Their  $K$  does not exceed 0.2, whereas in our case  $K$  is larger, as estimated from the velocity distributions in Fig. 12. For example, with the curves in Fig. 12, the velocity gradient in the wall region is about  $10 \text{ s}^{-1}$ , and  $K \sim 1.5$ , from Eqn. 5.10. We have been unable to find any published data on measurements of the lift force at this shear rate. If we extrapolate the results from Fig. 11(b) in Cao & Tamura (2008) to our  $K$  value, we obtain a lift coefficient due to shear effect  $C_{L0} \sim 1$ . In the present measurements, it is not practical to measure the shear effect for all situations. We will assume that the lift force induced by the shear effect is a constant of order  $C_{L0} \sim 1$  for all situations. We correct our measured lift coefficients by subtracting  $C_{L0}$ , and focus on the wall effects on the lift coefficient.

The lift coefficients  $C_L - C_{L0}$  are shown in Fig. 16 (b) plotted as a function of the normalized gap thickness  $G/2a$  for the various cylinders. The shear induced lift has been subtracted from the data. As before, the data obtained using different cylinders collapses and the lift coefficient increases with decreasing gap to diameter ratio. The increase of the lift coefficient contains two regions: weak increasing region for  $0.1 \lesssim G/2a \lesssim 1$ , and strong increasing region for  $G/2a \lesssim 0.1$ .

*Weakly increasing region:* As shown in Fig. 16(b), the lift coefficient changes from  $\sim 0$  to  $\sim 0.5$  when decreasing the gap to diameter ratio from 1 to 0.1, and the results for all cylinders follow this trend. The solid triangles represent the measurements by Nishino *et al.* (2007) of  $\text{Re} = 10^5$ . In their experiments, a uniform flow is established near the wall using a moving ground to eliminate shear effects. The lift coefficient for their non-rotating cylinder changes from around 0.05 to 0.4 when the gap to diameter ratio is decreased from 0.5 to 0.04. The lift coefficients in the present measurements agree very well with that in the measurements of Nishino *et al.* (2007) in this parameter region ( $0.1 \lesssim G/2a \lesssim 1$ ).

*Strongly increasing region:* Comparing with Nishino *et al.* (2007), we have more data for very small gap ratios, as shown in Fig. 16 (b). It clearly shows that the lift force further continues its increase with decreasing  $G/2a$  for  $G/2a \lesssim 0.1$ . An even more pronounced increase happens in this parameter region. The lift coefficient increases from 0.5 to around 4-5 when decreasing  $G/2a$  from 0.1 to 0.01. This means that the lift coefficient is highly sensitive to the vicinity of a wall, especially when the gap to diameter ratio becomes very small ( $G/2a \lesssim 0.1$  in the present case).

## 6. Conclusions

The motion of a heavy cylinder in a rotating drum filled with water was studied experimentally. The cylinder either co-rotated or counter-rotated with respect to the rotating drum depending on the chosen parameters. In co-rotation, the cylinder rolled along the wall at low drum rotation rates and began to slip with respect to the wall when the drum rotated faster. PIV measurements revealed that the slip motion was induced by the upward flow, which results from the blockage effect of the cylinder. With further increase of  $f_{drum}$ , the cylinder suddenly changed its direction of rotation and the counter-rotating cylinder floated above the wall. The transition is reflected in the rotating frequency of the cylinder, the azimuthal location of the cylinder, and the gap between it and the wall. Hysteresis was found in the dependence of these quantities on the drum frequency with proportionally large amounts for bigger cylinders. Detailed investigation showed that the counter-rotation motion was caused by the movements of the stagnation and separation points.

The velocity field without the inner cylinder was found to closely correspond to solid body rotation. However, the presence of the small cylinder effectively destroyed this state. The measure flow fields at different azimuthal distances from the small cylinder revealed the development of a steady quasi-stable flow with strongly reduced velocity, when compared with the solid-body rotation case.

For the counter-rotation, the cylinder rotated freely without contact with the drum wall as a result of the lift force acting on it. The drag and lift coefficients, on the freely counter-rotating cylinder, were measured in a wide range of Reynolds numbers  $2,500 < Re < 25,000$ , dimensionless rotation rates  $0.0 < \alpha < 1.2$ , and gap to diameter ratios  $0.003 < G/2a < 0.5$ . It was found that the drag coefficient is consistent with previous measurements on a cylinder in a uniform flow, and the drag coefficient is insensitive to the rotation motion of the cylinder and the vicinity of the wall next to the cylinder. However, a significant enhancement of the lift coefficient was observed in the present measurements. The measured lift coefficient strongly depends on the rotation motion of the cylinder and the vicinity of the wall. By comparing with previous experiments of a pure rotating cylinder without a wall, and a non-rotating cylinder near a wall, we found that the enhancement of the lift force is mainly caused by the vicinity to the wall.

We thank A. Prosperetti, J. J. Bluemink, and L. Botto for their stimulating discussions, Gert-Wim Bruggert and Martin Bos for building the experimental setup, and W. Schoonenbery and T.J.G. Jannink for assistance with the PIV measurements. This work was supported by STW, FOM & NWO.

## REFERENCES

- ASHMORE, J., DEL PINO, C. & MULLIN, T. 2005 Cavitation in a lubrication flow between a moving sphere and a boundary. *Phys. Rev. Lett.* **94**, 124501.
- BADR, H. M., COUTANCEAU, M., DENNIS, S. C. R. & MENARD, C. 1990 Unsteady flow past a rotating circular cylinder at reynolds numbers  $10^3$  and  $10^4$ . *J. Fluid Mech.* **220**, 459–484.
- BEARMAN, P.W. & ZDRAVKOVICH, M.M. 1978 Flow around a circular cylinder near a planar boundary. *J. Fluid Mech.* **89**, 33–47.
- BLUEMINK, J.J., LOHSE, D., PROSPERETTI, A. & VAN WIJNGAARDEN, L. 2008 A sphere in a uniformly rotating and shear flow. *J. Fluid Mech.* **600**, 201–233.
- BLUEMINK, J.J., LOHSE, D., PROSPERETTI, A. & VAN WIJNGAARDEN, L. 2010a Drag and lift forces on particles in a rotating flow. *J. Fluid Mech.* **643**, 1–31.
- BLUEMINK, J.J., PROSPERETTI, A. & VAN WIJNGAARDEN, L. 2010b Hydrodynamic interactions between identical spheres in a solid body rotating flow. *unpublished* .

- CAO, S. & TAMURA, Y. 2008 Flow around a circular cylinder in linear shear flows at subcritical reynolds number. *J. Wind Engineering and Industrial Aerodynamics* **96**, 1961–1973.
- CLIFFE, K.A. & TAVENER, S.J. 2004 The effect of cylinder rotation and blockage ratio on the onset of periodic flows. *J. Fluid Mech.* **501**, 125–133.
- CLIFT, R., GRACE, J.R. & WEBER, M.E. 1978 *Bubbles, Drops, and Particles*. Dover publications, Inc. New York.
- DAVIS, J. E., EDGE, B. L. & CHEN, H-S. 2007 Investigation of unrestrained cylinders rolling in steady uniform flow. *Ocean Eng.* **34**, 1431–1448.
- GOLDSTEIN, S. 1965 *Modern Developments in Fluid Dynamics, Vol. 1*. Edited by S. Goldstein, Dover publications, Inc.
- HU, H. H. 1995 Motion of a circular cylinder in a viscous liquid between parallel plates. *Theoret. Comput. Fluid Dynamics* **7**, 441–455.
- JEFFREY, D.J. & ONISHI, Y. 1981 The slow motion of a cylinder near to a plane wall. *Quarterly J. Mechanics Appl. Math.* **34**, 129–137.
- JEFFREY, G. 1922 The rotation of two circular cylinders in a viscous fluid. *Proc. Roy. Soc. Lond. A* **101**, 169–74.
- KANO, I. & YAGITA, M. 2002 Flow around a rotating circular cylinder near a moving plane wall. *Japan Society of Mech. Eng.* **45**, 259–268.
- LABRAGA, L., KAHISSIM, G., KEIRSBULCK, L. & BEAUBERT, F. 2007 An experimental investigation of the separation points on a circular rotating cylinder in cross flow. *J. Fluids Eng.* **129**, 1203–1211.
- LOHSE, D. & PROSPERETTI, A. 2003 Controlling bubbles. *J. Phys. Condens. Matter* **15**, 415–420.
- MAGNAUDET, J. & EAMES, I. 2000 The motion of high-reynolds-number bubbles in inhomogeneous flow. *Annu. Rev. Fluid Mech.* **32**, 659–708.
- MITTAL, S. 2003 Flow control using rotating cylinders: Effect of gap. *J. Appl. Mech. - Transactions of the ASME* **70**, 762–770.
- MITTAL, S. & KUMAR, B. 2003 Flow past a rotating cylinder. *J. Fluid Mech.* **476**, 303–334.
- NACIRI, M. A. 1992 Contribution à l'étude des forces exercées par un liquide sur une bulle de gaz: portance, masse ajoutée et interactions hydrodynamiques. *PhD thesis, L'Ecole Central de Lyon*.
- VAN NIEROP, E.A., LUTHER, S., BLUEMINK, J.J., MAGNAUDET, J., PROSPERETTI, A. & LOHSE, D. 2007 Drag and lift forces on bubbles in a rotating flow. *J. Fluid Mech.* **571**, 439–454.
- NISHINO, T., ROBERTS, G. T. & ZHANG, X. 2007 Vortex shedding from a circular cylinder near a moving ground. *Phys. Fluids* **19**, 025103.
- PROKUNIN, A. N. 2003 On a paradox in the motion of a rigid particle along a wall in a fluid. *Fluid Dynamics* **38**, 443–457.
- PROKUNIN, A. N. 2004 Microcavitation in the slow motion of a solid spherical particle along a wall in a fluid. *Fluid Dynamics* **39**, 771–778.
- SEDDON, J.R.T. & MULLIN, T. 2006 Reversal rotation of a cylinder near a wall. *Phys. Fluids* **18**, 041703.
- STEWART, B.E., HOURIGAN, K., THOMPSON, M. & LEWEKE, T. 2006 Flow dynamics and forces associated with a cylinder rolling along a wall. *Phys. Fluids* **18**, 111701.
- STEWART, B.E., THOMPSON, M.C., LEWEKE, T. & HOURIGAN, K. 2010 Numerical and experimental studies of the rolling sphere wake. *J. Fluid Mech.* **643**, 137–162.
- SUMNER, D. & AKOSILE, O.O. 2003 On uniform planar shear flow around a circular cylinder at subcritical reynolds number. *J. Fluids and Structures* **18**, 441–454.
- TAKAYAMA, S. & AOKI, K. 2004 Flow characteristics around a rotating circular cylinder. *Proc. Schl. Eng. Tokai Univ. Ser. E* **29**, 9–14.
- TOKUMARU, P.T. & DIMOTAKIS, P.E. 1991 Rotary oscillation control of a cylinder wake. *J. Fluid Mech.* **224**, 77–90.
- TOKUMARU, P.T. & DIMOTAKIS, P.E. 1993 The lift of a cylinder executing rotating motions in a uniform flow. *J. Fluid Mech.* **255**, 1–10.
- YANG, L., SEDDON, J.R.T., MULLIN, T., DEL PINO, C. & ASHMORE, J. 2006 The motion of a rough particle in a stokes flow adjacent to a boundary. *J. Fluid Mech.* **557**, 337–346.
- ZDRAVKOVICH, M.M. 1985 Forces on a circular cylinder near a plane wall. *Applied Ocean Research* **7**, 197–201.